Proceedings of the 21st ICSMGE, Vienna, Austria, 14 – 19 June 2026. Pistrol, Adam & Schweiger (eds.)
Published by: ÖGG, Austrian Society for Geomechanics, Salzburg, Austria, ISBN 978-3-9503898-4-5
https://doi.org/10.53243/ICSMGE2026-2291

Compaction degree distribution dependency on embankment shape due to roller compaction

Katsuyuki Kawai, Koji Nakashima
Department of Civil and Environmental Engineering, Kindai University, Higashi-Osaka, Japan,
kkawai@civileng.kindai.ac.jp

ABSTRACT: Large-scale embankments are typically constructed using roller compaction. Compaction is fundamentally governed by the initial and boundary value problem of ground materials modeled as a three-phase mixture. Roller compaction, involving loading due to moving rollers, introduces further complexity to the stress-strain distribution within the embankment. In this study, compaction is conceptualized as a loading and unloading process on unsaturated soil under water-undrained and air-drained conditions. The compaction process is simulated using a coupled finite element analysis framework for soil, water, and air interactions. Initially, static compaction under one-dimensional compression conditions was simulated to validate the definition of compaction. The results yield consistent compaction curves in terms of water content and dry density. Subsequently, the effects of embankment geometry on compaction were investigated by modeling the roller compaction process as a boundary value problem. The findings reveal that the degree of compaction within the embankment is influenced by the initial rolling direction. For embankments constructed on horizontal foundations, the directional dependency diminishes after repeated rolling. However, in valley-filled embankments, this dependency persists, and heterogeneity becomes more pronounced with irregular valley-filled embankment foundations. Moreover, the degree of compaction varies with depth within a compacted layer, leading to inevitable gaps in compaction degree between layers during multi-layer compaction. This discrepancy is especially evident in thick layers, where localized variations in soil parameters, such as permeability coefficients, are observed. The study further highlights that higher water content exacerbates the localization of compaction effects, emphasizing the critical importance of water content management during compaction.

KEYWORDS: Roller compaction, compaction degree distribution, soil/water/air coupled simulation

1 INTRODUCTION

As the scale of embankment construction projects grows, roller compaction using heavy machinery has become the predominant method for construction. Roller compaction applies moving loads using principal stress rotation to geomaterials, which behave as elasto-plastic materials. This process can result in the localization of strain and stress within the embankment. Kawai et al. (2021) conducted a roller compaction model test, as shown in Figure 1, and analyzed the distribution of compaction degree using X-ray CT images. Figure 2 displays the CT images for this study and the average brightness values within the highlighted rectangular areas. In these CT images, lower brightness values indicate higher density. These findings revealed that the compaction degree tends to increase at the terminal ends of the roller compaction direction, a phenomenon attributed to shear deformation induced by roller compaction and constraints imposed by the soil box walls.

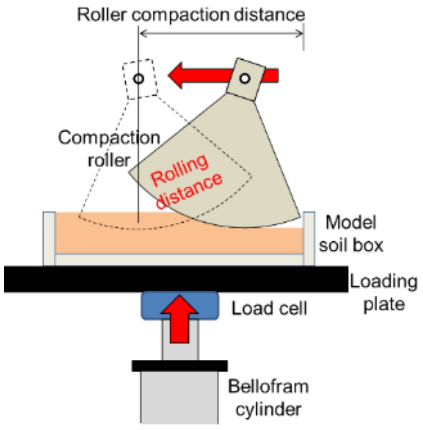

Figure 1. Overview of the roller compaction model test

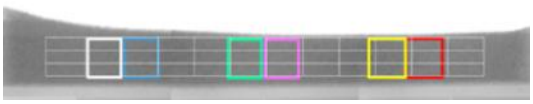

60.79	62.22	62.13	64.34	63.32	64.44
59.99	60.20	61.68	63.10	61.62	63.98
59.51	59.83	61.88	62.68	60.55	62.59

Figure 2. CT images and brightness value distribution of the model soil tank after rolling

In Japan, where mountainous regions are prevalent, the construction of linear embankments such as roads and railways involve traversing various terrain conditions. Consequently, embankments are built with geometries that align with the underlying terrain, leading to localization of compaction degree caused during the roller compaction process. The non-uniformity of compaction degree can result in localized permeability within the embankment, potentially generating perched water that triggers minor slope failures. Therefore, compaction work that accounts for geometric boundary conditions is deemed necessary to ensure the long-term stability and quality of embankments. This study aims to elucidate the trends in compaction degree distribution during compaction work through simulations that accurately represent the compaction behavior resulting from the interactions within geomaterials that occur among soil particle skeletons, pore water, and pore air.

2 COUPLED PROBLEM OF SOIL, WATER, AND AIR, AND STATIC COMPACTION SIMULATION

To understand the effects of compaction, it is necessary to model the interactions among the soil particle skeleton, pore water, and pore air within geomaterials. However, modeling geomaterials as a three-phase mixture is challenging, and resultingly, compaction has not been explained within the framework of soil mechanics. "Compaction" is defined as the process of increasing the density of geomaterials by applying external forces to expel air phases. It can be modeled as the compression and unloading of unsaturated geomaterials under undrained conditions. In this study, compaction is represented

as the result of an initial and boundary value problem by performing soil-water-air coupled analyses incorporating the constitutive model for unsaturated soil.

2.1 *Mechanical models applied in the coupled soil-water-air finite element analysis code*

In this study, the finite element analysis code DACSAR-MP is employed, which is capable of representing the interactions among the soil particle skeleton, pore water, and pore air. The effective stress for unsaturated soils is expressed by the following equation.

$$\boldsymbol{\sigma}' = \boldsymbol{\sigma}^{net} + p_s \mathbf{1} \tag{1}$$

$$\boldsymbol{\sigma}^{net} = \boldsymbol{\sigma} - p_a \mathbf{1},\ p_s = S_e s \tag{2}$$

$$s = p_a - p_w,\ S_e = \frac{S_r - S_{rc}}{1 - S_{rc}} \tag{3}$$

Here, $\boldsymbol{\sigma}'$ is the effective stress tensor; $\boldsymbol{\sigma}^{net}$ is the net stress tensor; $\mathbf{1}$ is the unit tensor; $\boldsymbol{\sigma}$ is total stress tensor; s is suction; p_s is suction stress; p_a is pore air pressure; p_w is pore water pressure; S_r is degree of saturation; S_e is the effective degree of saturation; and S_{rc} is the asymptote degree of saturation at $s \to \infty$. The yield function is expressed as follows.

$$f\left(\boldsymbol{\sigma}', \zeta, \varepsilon_v^p\right) = MD \ln \frac{p'}{\zeta p'_{sat}} + \frac{MD}{n_E}\left(\frac{q}{Mp'}\right)^{n_E} - \varepsilon_v^p = 0 \tag{4}$$

$$\zeta = \exp\left[(1 - S_e)^{n_s} \ln a\right],\ MD = \frac{\lambda - \kappa}{1 + e_0} \tag{5}$$

$$p' = \frac{1}{3}\boldsymbol{\sigma}' : \mathbf{1},\ q = \sqrt{\frac{3}{2}\mathbf{s} : \mathbf{s}},\ \mathbf{s} = \boldsymbol{\sigma}' - p'\mathbf{1} = \mathbf{A} : \boldsymbol{\sigma}',\ \mathbf{A} = \mathbf{I} - \frac{1}{3}\mathbf{1} \otimes \mathbf{1} \tag{6}$$

Here, ε_v^p is the plastic volumetric strain; M is q/p' at the critical state; D is the dilatancy coefficient; e_0 is the initial void ratio; a, n_s, and n_E are shaping parameters of the yielding surface; λ and κ are the compression and expansion index, respectively. The yielding surface can be expressed as Figure 3 on space of $p' \sim q \sim S_e$. The constitutive equation can be obtained from equation (4) as follows.

$$\boldsymbol{\sigma}' = \mathbf{D} : \boldsymbol{\varepsilon} - \mathbf{C} \cdot \dot{S}_e \tag{7}$$

Here, $\mathbf{D}$ is the elasto-plastic stiffness matrix; $\boldsymbol{\varepsilon}$ is a strain tensor; and $\mathbf{C}$ is the tensor indicating stiffness change due to desaturation. The continuous equation of pore water and air is expressed as equation (8) and (9), respectively.

$$n\dot{S}_r - S_r \dot{\varepsilon}_v + \mathrm{div}\tilde{\mathbf{v}}_\mathbf{w} = 0 \tag{8}$$

$$\left(1 - S_r\right)\dot{\varepsilon}_v + n\dot{S}_r - n\left(1 - S_r\right)\frac{\dot{p}_a}{p_a + p_0} - \mathrm{div}\tilde{\mathbf{v}}_\mathbf{a} = 0 \tag{9}$$

Here, n is porosity; $\tilde{\mathbf{v}}_\mathbf{w}$ and $\tilde{\mathbf{v}}_\mathbf{a}$ is the relative velocity of pore water and air, respectively; ε_v is volumetric strain; and p_0 is atmospheric pressure. Unsaturated permeability of water and air is expressed as follows in the Mualem equation and van Genuchten equation.

$$k_{rw} = S_e^{1/2}\left[1 - \left(1 - S_e^{1/m}\right)^m\right]^2 \tag{10}$$

$$k_{ra} = \left(1 - S_e\right)^{1/2}\left(1 - S_e^{1/m}\right)^{2m} \tag{11}$$

Here, k_{rw} and k_{rw} are the relative unsaturated permeability of water and air, respectively, and m is a shaping parameter.

2.2 *Static compaction simulation*

To verify that compaction can be represented using soil-water-air coupled analysis, a simulation of a static compaction test was conducted. Figure 4 illustrates the analysis mesh and boundary conditions. A one-dimensional compression model was employed, with only the compaction load application surface defined as an air-permeable boundary. Table 1 summarizes the input parameters for the simulations, and Figure 5 shows the soil water retention characteristic curves

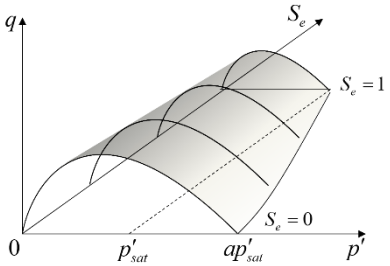

Figure 3. Yielding surface for unsaturated soil

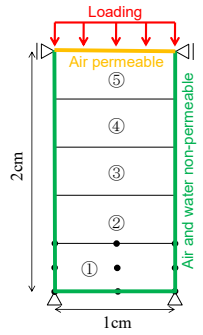

Figure 4. Analysis mesh and boundary conditions for static compaction simulations

Table 1. Material parameters for simulation

λ	κ	k_w (m/sec)	M
0.107	0.011	1.157×10^{-7}	1.344
a	n_s	k_a (m/sec)	m
30	1.0	1.157×10^{-5}	0.8

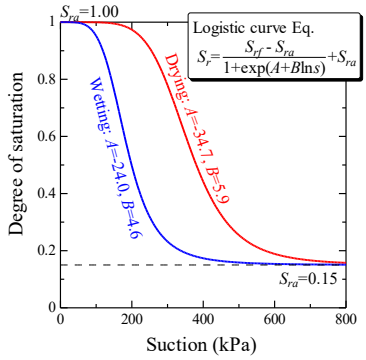

Figure 5. Water retention characteristics for simulation

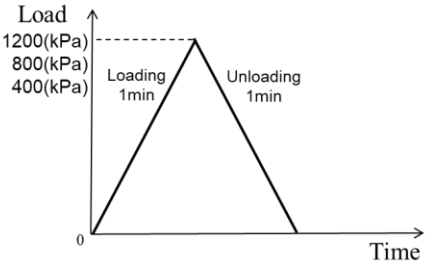

Figure 6. Loading condition

used. The initial void ratio was set to 0.85, and the initial degree of saturation was calculated based on water content, corresponding to suction on the primary wetting curve as the initial water retention state. The compaction load history, shown in Figure 6, was applied. Element 1 is the farthest element from the air-permeable boundary, and it is considered to have the least compaction effect. Figure 7 shows the changes in void ratio for element 1. At the initial stage of loading, soils with lower water content tend to exhibit higher stiffness, making them less compressive. However, as the water content increases, the compression progresses, and the soils become less deformable. It was also observed that soils exhibiting this trend did not follow linear elastic behavior during unloading and expansion.

The changes in suction during this process are shown in Figure 8. The figure also presents the changes in pore water pressure and pore air pressure over time. When the water content is low, corresponding to a low degree of saturation, the air permeability is high according to Equation (11). As a result, pore air is easily expelled during compression. However, as the water content increases and the degree of saturation becomes higher, the air permeability decreases. This is particularly evident in element 1, which is located far from the air permeable boundary. Here, trapped pore air leads to a rise in air pressure during compression, as observed in Figure 8. Under undrained conditions, pore water pressure rises and falls in response to loading and unloading. However, changes in pore air pressure influence suction behavior, leading to volume changes that depend on the water content, as illustrated in Figure 7. Consequently, a compaction curve with a convex shape relative to the water content, as shown in Figure 9, is obtained from numerical simulation. It is evident that higher compaction loads result in larger maximum dry densities at lower optimum water contents, accurately reproducing the actual compaction test results. The dashed contours in Figure 9 further indicate the maximum load observed in multiple static compaction tests conducted by Kawai et al. (2002). The compaction curves obtained from numerical simulations under constant loads align well with these experimental results.

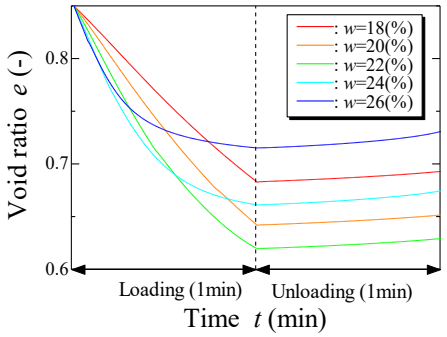

Figure 7. Changes in void ratio of element 1

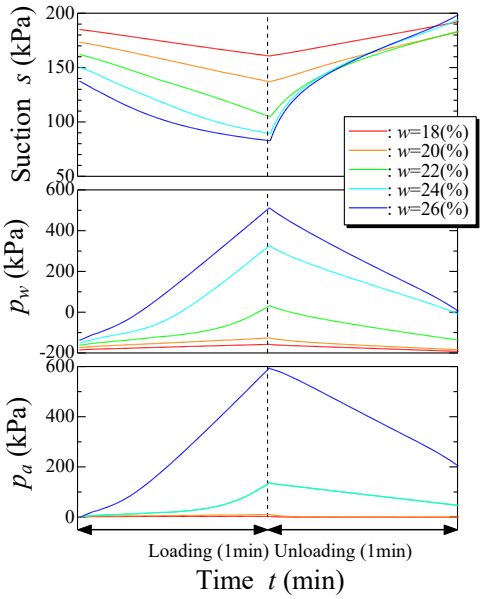

Figure 8. Changes in water and air pressure during compaction for element 1

3 ROLLER COMPACTION SIMULATIONS

Static compaction test simulations successfully expressed the behavior observed in laboratory compaction tests. However, in practical applications, the boundary value problems are much larger in scale and involve dynamic compaction processes, such as roller compaction, which induces localized shear stresses due to moving loads. This suggests that compaction quality depends on the rolling procedure employed. Using the same material parameters as in the static compaction tests, roller compaction was thus simulated for three types of embankments, as illustrated in Figure 8. The objective was to clarify the distribution trends of compaction degree based on embankment geometry.

3.1 *Analysis conditions*

Figure 10 (a) depicts an embankment on a horizontal foundation, while Figures 10 (b) and (c) illustrate valley-fill embankments, each with distinct displacement boundary conditions. Similar to the static compaction simulation, only the roller compaction surface was subjected to an air permeable boundary under water undrained conditions. In the figures, a two-layer compaction approach is assumed, with the orange dashed lines indicating the boundary between layers. Initially, the material water content was set, and the corresponding degree of saturation and suction along the boundary wetting curve was used to provide the initial water retention state. The lower layer of embankment was generated, and a distributed

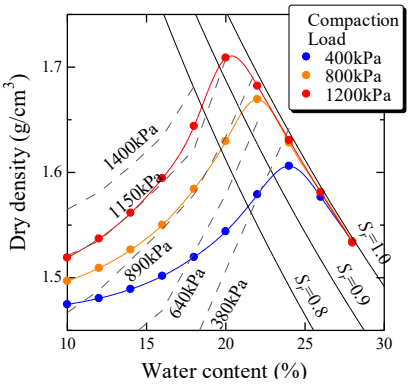

Figure 9. Compaction curves obtained from static compaction simulations

load was applied as a moving load on the top surface, as shown in Figure 11. The compaction load history for each element during this process is illustrated in Figure 11 (b). The loading and unloading history in roller compaction differs, even when applying the same magnitude of loading as the static compaction simulation. For each layer, roller compaction consisted of two rolling compactions back and forth. After the compaction of the lower layer, the air-drainage boundary on the top surface was removed, and the upper layer was generated.

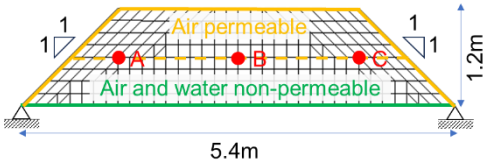

(a) Embankment on a horizontal foundation

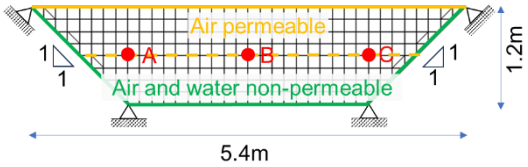

(b) Symmetric valley-fill embankment

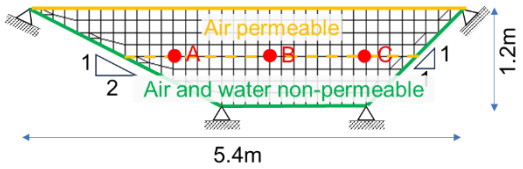

(c) Asymmetric valley-fill embankment

Figure 10. Analysis mesh and boundary conditions for roller compaction simulation

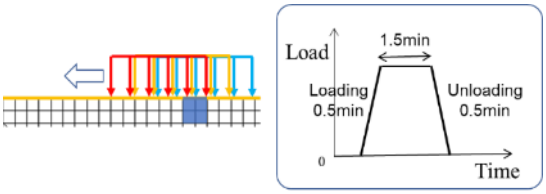

Figure 11. Loading condition and load history per element for roller compaction simulations

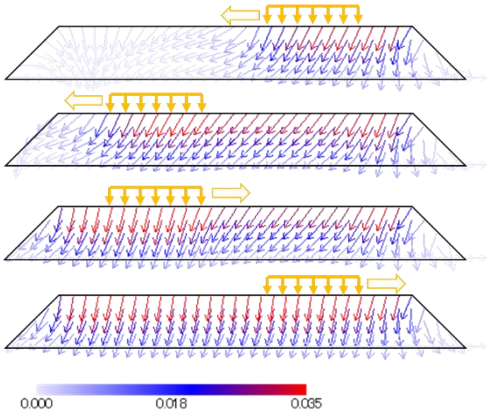

Figure 12. Distribution of displacement during roller compaction on a horizontal foundation (400kPa roller compaction @ w=20%)

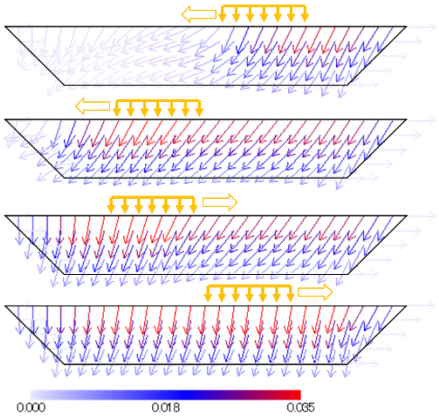

Figure 13. Distribution of displacement during roller compaction on a symmetric valley-fill (400kPa roller compaction @ w=20%)

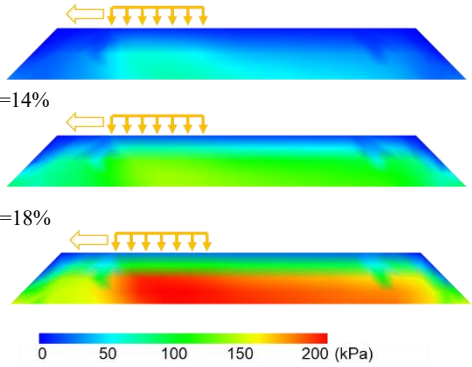

(a) w=14%

(b) w=18%

(c) w=20%

Figure 14. Distribution of air pressure during roller compaction on a horizontal foundation (400kPa roller compaction)

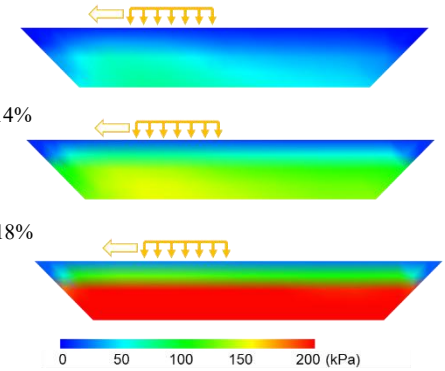

(a) w=14%

(b) w=18%

(c) w=20%

Figure 15. Distribution of air pressure during roller compaction on a symmetric valley-fill (400kPa roller compaction)

The rolling load was then applied to the top surface of the upper layer in the same manner. To account for the influence of the direction of roller compaction, two initial rolling conditions were considered: rolling from the left end of the embankment (initial rightward rolling) and rolling from the right end (initial leftward rolling). Additionally, to evaluate the impact of layer thickness, a separate condition with single-layer roller compaction for the entire embankment was generated. In the single layer case, the load history was maintained by performing four rolling compactions back and forth.

3.2 *Simulation results and discussions*

Figures 12 and 13 illustrate the displacement distributions during the first forward-and-backward roller compaction pass for embankments on a horizontal foundation and for valley-fill embankments, respectively. The figures also indicate the rolling load position and its direction. In both cases, during the forward pass of the rolling load, displacements occur in the rolling direction as the load approaches. When the load passes directly overhead, significant vertical compression occurs, causing the displacement vector to point downward. After the load passes, unloading expansion reduces the vertical component, resulting in a displacement distribution tilted toward the rolling direction. In the return pass, displacements initially tilted in the initial forward direction (leftward) adjust vertically, but residual displacements remain biased toward the initial rolling direction. For embankments on a horizontal foundation, deformation tends to remain at the front face of the slope. In contrast, for a

valley-fill embankment, horizontal displacements in the rolling direction are constrained. Figures 14 and 15 show the distribution of pore air pressure during compaction for materials with different water contents. Regardless of the embankment type, higher water content results in greater residual air pressure. The highest air pressure is observed directly beneath the applied load, and the air pressure dissipates after the load passes. In embankments constructed on a horizontal foundation, the dissipation of air pressure after load passage is evident because the crest and slopes work as air-permeable boundaries. However, in valley-fill embankments, residual air pressure remains trapped at the base, indicating incomplete dissipation. Figures 16 and 17 show the trajectories for nodes A, B, and C first presented in Figure 10. In Figure 16 and 17 solid lines represent leftward rolling and dashed lines represent rightward rolling. The plotted points indicate the state of the nodes at the end of the first layer compaction. In embankments on a horizontal foundation (Figure 16), all nodes exhibit the largest horizontal movement during the forward (leftward) pass of the initial rolling. Subsequently, they compress while tilted toward the rolling direction. The central node moves vertically downward, while nodes A and C, located near the slope, move toward the slope front with larger vertical displacements than the center node. After the forward rolling pass, the displacement behavior becomes nearly symmetric. In valley-fill embankments (Figure 17), horizontal movement is constrained at the edge in the initial rolling direction, reducing leftward movement. However, the displacement distribution overall remains biased toward the initial rolling direction. Figures 18 and 19 show the vertical displacement of the top surface of the first layer after the roller compaction load passes both ends (blue and red lines) and upon completing the second layer compaction (green line). The embankment center is indicated by a dashed line. For embankments on a horizontal foundation (Figure 18), the compression near the shoulder of where the initial roller compaction starts is pronounced due to compaction of the first layer. However, because the upper layer rolling load does not directly act above the shoulder, the

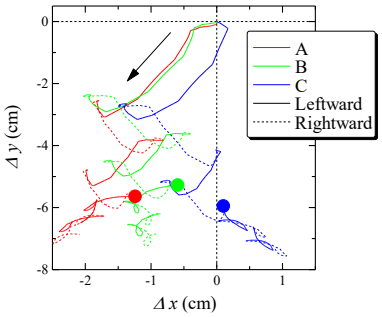

Figure 16. Node trajectories during roller compaction on a horizontal foundation (400kPa@w=20%)

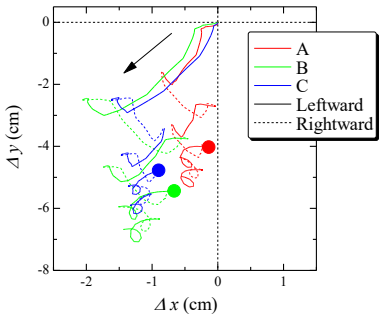

Figure 17. Node trajectories during roller compaction on a symmetric valley-fill (400kPa@w=20%)

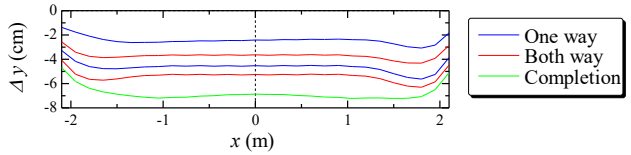

Figure 18. Settlement of the upper surface of the first layer of the embankment on a horizontal foundation (400kPa@w=20%)

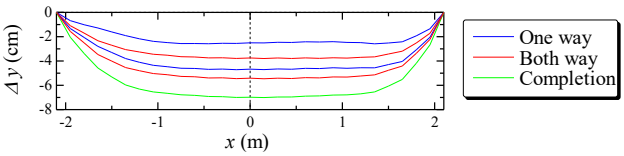

Figure 19. Settlement of the upper surface of the first layer of a symmetric valley-fill (400kPa@w=20%)

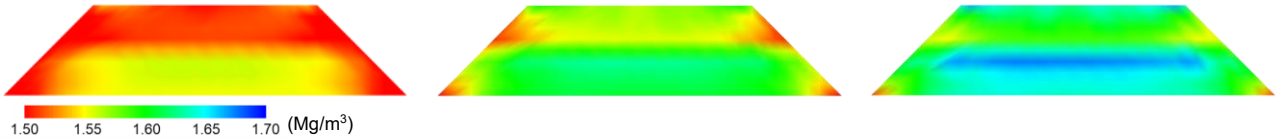

(a) w=14% (b) w=18% (c) w=20%

Figure 20. Distribution of dry density in embankment on a horizontal foundation (400kPa)

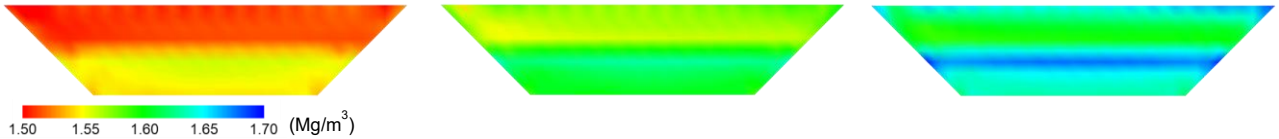

(a) w=14% (b) w=18% (c) w=20%

Figure 21. Distribution of dry density in a symmetric valley-fill (400kPa)

(a) w=14% (b) w=18% (c) w=20%

Figure 22. Distribution of dry density in a symmetric valley-fill with single layer compaction (400kPa)

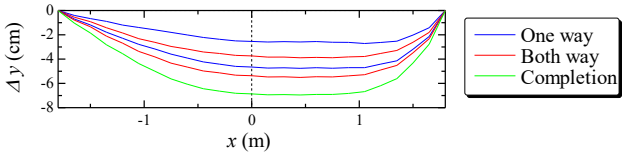

Figure 23. Settlement of the upper surface of the first layer of an asymmetric valley-fill (initial leftward roller compaction 400kPa@w=20%)

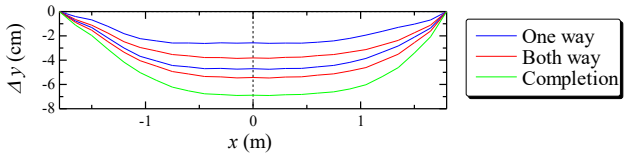

Figure 24. Settlement of the upper surface of the first layer of an asymmetric valley-fill (initial rightward roller compaction 400kPa @w=20%)

compression is relatively uniform upon embankment completion. On valley-fill embankments (Figure 19), greater compression occurs in the central area, where the soil layer is thicker. Although the range of uniform compression expands by embankment completion, more non-uniform settlement is evident compared to horizontal foundation embankments. It should be noted that even after embankment completion, the tendency for greater compression at the initial rolling start point (right end) persists. This indicates that the rolling load does not produce perfectly symmetric compaction, even with repeated rolling passes.

Figures 20 and 21 compare the dry density distributions at embankment completion for the horizontal foundation and in the valley-fill embankment at various water contents. The dry densities are generally higher than those obtained in static compaction simulations (Figure 9), indicating an increase in compaction degree due to repeated rolling. While the upper layer has lower dry densities due to fewer rolling passes, the highest dry density regions locally appear around the boundary between the upper and lower layers. This trend of localized compaction becomes more pronounced at higher water contents. In real embankments, such compaction layer boundaries can lead to generation of perched water. Additionally, for valley-fill embankments, the dry density distribution near the surface is asymmetric and dependent on the initial rolling direction. For comparison, Figure 22 shows the dry density distribution for single-layer compaction of a valley-fill embankment. Greater layer thickness leads to more pronounced depth-dependent dry density differences and asymmetric compaction near the surface, with the compaction degree distribution influenced by the initial rolling direction. When constructing embankments using multilayer compaction, discrepancies in the degree of compaction between layers are inevitable. It follows, therefore, that increasing the thickness of each layer exacerbates the non-uniformity of compaction degree within the embankment.

The dependency on the initial rolling direction is more pronounced in valley-fill embankments with asymmetric foundations. Figures 23 and 24 compare the vertical displacement of the top surface of the first layer for different initial rolling directions as shown in Figure 10 (c). In valley-fill embankments, compression settlement at both ends of the layer is smaller due to thinner layers, while compression at the rolling start point is larger (Figure 19). This tendency is more significant when rolling starts from the thicker to the thinner side (initial leftward rolling, Figure 23). In contrast, initial rightward rolling compensates for the asymmetric valley-fill, resulting in a more symmetric compression settlement (Figure 23).

4 CONCLUDING REMARKS

In this study, the effects of embankment geometry on compaction efficiency were investigated using boundary value problems modeled with soil-water-air coupled finite element analysis for roller compaction processes. The results confirmed that the degree of compaction within the ground depends on the initial rolling direction. For embankments on a horizontal foundation, the dependency on the rolling direction diminishes after repeated forward and backward rolling passes. However, for valley-fill embankments, the dependency on the initial rolling direction persists. For valley-fill embankments on irregular foundations, the influence of the initial rolling direction becomes more pronounced. Additionally, depth-dependent distribution in compaction degree occur within compacted layers, making gaps in compaction degree between layers inevitable in multi-layer compaction. Therefore, for multi-layered roller compaction with thick layers, localized distributions in soil properties, such as permeability coefficients, are anticipated. Moreover, such localized compaction due to roller compaction becomes more pronounced at higher water contents, emphasizing the importance of water content management during compaction construction.

5 REFERENCES

Kawai, K., Arinishi, K. and Nakashima, K. 2021. Compaction degree distribution induced by roller compaction with using soil/water/air coupled F. E. simulation. *Journal of JSCE* A2 77(2), I_263-I_273 (in Japanese).

Kawai, K., Kim, E., Nagareta, H., Iizuka, A. and Honda, M. 2002. A simple method to predict the consolidation yield stress of compacted soils considering suction effects in unsaturated soil media. *Journal of Applied Mechanics* 5, 785-792 (in Japanese).

Mualem, Y. 1976. A new model for predicting the hydraulic conductivity of unsaturated porous media. *Water Resources Research* 12(3), 514-522.

Sugiyama, Y., Kawai, K. and Iizuka, A. 2016. Effects of stress conditions on B-value measurement. *Soils and Foundations* 56(5), 848-860.

van Genuchten. 1980. A closed-form equation for predicting hydraulic conductivity of unsaturated soils. *Soil Science Society American Journal* 44, 892-898.